ACOLITE processing for Sentinel-2 and Landsat-8: atmospheric correction and aquatic applications

Quinten Vanhellemont*, Kevin Ruddick

Royal Belgian Institute of Natural Sciences, Operational Directorate Natural Environments, Gulledelle 100, 1200 Brussels, Belgium

Abstract

Inland and coastal water monitoring is entering a new era thanks to the free availability of Landsat 8 and Sentinel-2A imagery. Whereas moderate resolution ocean color sensors typically have a resolution between 250 m and 1 km, and can often not be used in the near-shore environment, these new satellite missions provide data at more relevant spatial scales of 10 to 60 m. This spatial resolution allows the direct observation of human activities and their impacts, such as offshore construction, dredging operations, and island building activities. With a ten day revisit, and four 10 m visible and NIR channels and a 20 m red-edge band, S2A brings a new set of observations at unprecedented spatial and temporal coverage. S2A also shows new potential for chlorophyll a mapping in near-shore coastal and inland waters. We present here updates to the ACOLITE atmospheric correction for S2A/MSI. We show a good correspondence of the two systems using same-day L8 and S2A imagery over the Markermeer in the Netherlands. By using both L8 and S2A missions as a virtual constellation, drawbacks associated with the low temporal revisit of the satellites (respectively 16 and 10 days), can be reduced. The virtual constellation improves lack of coverage due to clouds and is better able to track rapid changes in the environment. The red-edge band on S2A/MSI allows the mapping of chlorophyll a red absorption, and hence chlorophyll a concentration at new spatial and temporal scales.

Keywords: water quality, dredging, algal blooms, remote sensing, Landsat 8, Sentinel-2, constellation

1. Introduction

The launch of the Operational Land Imager (OLI) on board of Landsat 8 in 2013 has sparked a new interest of the water quality remote sensing community in high resolution imagery, not only due to its improved radiometric quality (Pahlevan et al., 2014; Franz et al., 2015), essential for water remote sensing, but also thanks to the open data policies used by the space agencies. The first of the Copernicus high resolution optical satellites, Sentinel-2A (S2A), was launched in June 2015, and is now reliably providing free data. The MultiSpectral Imager (MSI) on S2A provides some advantages over the OLI with higher resolution (10 m compared to 30 m on OLI) visible and near-infrared bands, and an additional red-edge band at 705 nm, useful for quantifying the red light absorption by chlorophyll a.

The usefulness of high spatial resolution sensors (10-60m) for monitoring coastal and inland waters has become apparent with new applications quickly emerging. At these spatial scales "new" processes can be resolved from space, including human activities and their impacts, such as dredging (Barnes et al., 2015; Vanhellemont and Ruddick, 2015) and offshore construction (Vanhellemont and Ruddick, 2014). Turbid river plumes can be analysed in more detail thanks to the high spatial resolution and robust atmospheric correction using shortwave-infrared bands (Brando et al., 2015; Ody et al., 2016), and retrieval of various optically active constituents is possible (Concha and Schott, 2016). In the southern North Sea, shipwrecks were detected in Landsat 8 imagery by analysing turbid tidal wakes (Baeye et al., 2016), and wide-spread damage to coral reefs was found associated with island building in the South China Sea (Barnes and Hu, 2016).

The red-edge band on S2A/MSI is of importance for European Monitoring under the Water Framework Directive (WFD, 2000/60/EC and amendments). The WFD directive requires EU member states to monitor inland and near-shore (within the first nautical mile) coastal waters. These waters present large challenges

*Corresponding author:
quinten.vanhellemont@naturalsciences.be

for typical monitoring systems, both for in situ and remote sensing components. For traditional ocean colour sensors (SeaWiFS, MODIS, MERIS, VIIRS, OLCI) these areas present a problem mainly in terms of spatial extent (where 250 m to 1 km pixel sizes are insufficient), but also in terms of atmospheric correction as these sensors lack good quality SWIR bands. The Sentinel-2 mission has potential to improve monitoring capabilities in these waters, thanks to its short-wave infrared bands for atmospheric correction, and the presence of a red-edge band, allowing estimation of chlorophyll a absorption. First indications show good performance of the red-edge band on S2A/MSI and hence the possibility of chlorophyll a concentration retrieval in coastal and inland waters (Vanhellemont and Ruddick, 2016; Toming et al., 2016). Thanks to its wide swath of 290 km, a single satellite can acquire all land and coastal areas every ten days. At higher latitudes the swaths of different relative orbits will overlap and the temporal coverage is increased to two or more acquisitions every ten day cycle. When the second Sentinel-2 satellite will be launched in 2017, the revisit time will improve to five days for global cover, and at higher latitudes, multiple images per week will be acquired.

In the present paper we present:

- an update of the ACOLITE atmospheric correction for S2A, and an evaluation of the performance of both L8/OLI and S2A/MSI,
- the use of both satellite sensors in tandem, in order to improve temporal coverage, reduce the impact of cloud cover, and combine the information captured by both sensors, and
- the use of the new red-edge band on S2A/MSI for detecting and mapping intense phytoplankton blooms in coastal and inland waters, and the opportunities presented for water quality monitoring requirements.

2. Data and Methods

2.1. Study region

The Markermeer (MM) is a shallow (3–5 m depth) artificial lake in the Netherlands, with a large surface area (700 km^2). The MM was created in the IJsselmeer by the construction of an artificial dam, the Houtribdijk, between 1963–1975. The lake is highly turbid thanks to its shallow depth and wind-induced sediment resuspension (Kelderman et al., 2012; Eleveld, 2012), and is characterised by a high chlorophyll a concentration (Vos et al., 2003) that is steadily increasing since the 1990s (Lammens, 1999). High turbidity and chlorophyll concentration have negative impacts on fish and bird populations, mainly due to a change in nutrient regime and a shift towards phosphorus-limited phytoplankton (Noordhuis, 2010, 2014). In 2016 the construction of the Marker Wadden (MW) project was started. The MW project aims to improve overall water and ecosystem quality in the MM, by increasing the extent of natural shores, mud flats, and marshlands in the lake (Natuurmonumenten, 2016). With high resolution imagery from L8 and S2 we were able to follow construction and dredging works from space, and estimate turbidity and the extent of the dredging plumes. Figure 1 shows the Markermeer - with the newly constructed Marker Wadden island - and the IJsselmeer separated by the Houtribdijk, as observed by Sentinel-2A on 2016-09-25.

2.2. Satellite data

Satellite data from L8/OLI and S2A/MSI were acquired respectively from the EarthExplorer (USGS, 2016) and the Copernicus SciHub (ESA/Copernicus, 2016) data portals. Data are provided by the space agencies as geographically projected Top-Of-Atmosphere (TOA) calibrated reflectances, hereafter TOA or L1 data. The sensors have a large overlap in the band set, with however significant differences in the relative spectral response function of the bands. While the panchromatic channel on OLI provides some interesting resolution improvements with sharpening techniques, it is not used in this study. The TOA data was processed to water-leaving radiance reflectances, hereafter water reflectances or ρ_w, using an updated ACOLITE processor (see section 2.3).

2.3. ACOLITE atmospheric correction

The atmospheric correction (AC) developed for L8/OLI by Vanhellemont and Ruddick (2014, 2015) was adapted to S2A/MSI. The AC assumes that due to extremely high pure-water absorption in the shortwave-infrared (SWIR) bands at 1.6 and 2.2 μm the signal remaining in these bands after Rayleigh correction is caused by aerosol scattering. The water-leaving radiance reflectance, ρ_w, is zero in the SWIR bands:

$$\rho_w^{1.6} = \rho_w^{2.2} = 0 \quad (1)$$

and thus, the Rayleigh and gas-corrected reflectance, ρ_{rc}, is equal to the multiple-scattering aerosol reflectance, ρ_{am}:

$$\rho_{rc}^{1.6} = \rho_{am}^{1.6} \quad \text{and} \quad \rho_{rc}^{2.2} = \rho_{am}^{2.2}. \quad (2)$$

The ratio of ρ_{am} in the two SWIR bands (ϵ) is used to extrapolate the aerosol reflectance to the visible and near-infrared bands. Vanhellemont and Ruddick (2015) used a simple exponential extrapolation which here is used as a baseline:

$$\epsilon = \frac{\rho_{am}^{1.6}}{\rho_{am}^{2.2}} \quad \text{and} \quad \epsilon^{\lambda} = \epsilon^{(2.2\mu m - \lambda)/(2.2\mu m - 1.6\mu m)} \tag{3}$$

The SWIR bands on S2A/MSI have a lower radiometric performance than those on L8/OLI and a 320 m spatial averaging of the SWIR bands is performed for MSI before the atmospheric correction (Vanhellemont and Ruddick, 2016). To reduce the impact of bright SWIR pixels (e.g. from ships, wave breaking, or land pixels) in the spatial averaged SWIR signal, a threshold masking is first perfomed at native resolution of the SWIR bands (20 m) to exclude pixels with a reflectance above 2.15% at 1.6 μm (Wang and Shi, 2006; Vanhellemont and Ruddick, 2015).

2.4. Turbidity algorithm

The turbidity algorithm of Nechad et al. (2009) was used, with a recalibration to L8/OLI and S2A/MSI spectral bands. The NIR bands were used for turbidity retrieval in the present study area, as the red band can be impacted by (1) non-linearity in cases of high turbidity, (2) bottom reflectance, and (3) by significant absorption by chlorophyll a during intense algal blooms. The algorithm has the form:

$$Turbidity(FNU) = \frac{A \times \rho_w}{1 - \frac{\rho_w}{C}}, \tag{4}$$

with ρ_w water reflectance in a single red or NIR band, and two calibration parameters A and C. The 835 and 865 nm bands on S2A/MSI and L8/OLI were used with calibration coefficients A = 1913.65 and 3431.36 gm^{-3} and C = 0.19130 and 0.21135 (calibration by B. Nechad, summer 2016). This resulted in Turbidity maps with 10 and 30 m spatial resolution for S2A and L8.

2.5. Chlorophyll algorithm

The chlorophyll algorithm of Gons et al. (2005) was used unmodified. The band ratio of the red-edge and red bands is used to retrieve chlorophyll a absorption a_{chl}:

$$a_{chl} = \left[(0.70 + b_b) \times (\frac{\rho_w^{705}}{\rho_w^{664}}) - 0.40 - b_b^{1.05} \right], \tag{5}$$

where b_b is the backscattering coefficient (m^{-1}) derived from the 782 nm band:

$$b_b = \frac{1.61 \times \rho_w^{782}}{0.082 - 0.6 \times \rho_w^{782}}. \tag{6}$$

Chlorophyll a concentration can then be derived by assuming a mass specific chlorophyll a absorption (a^*_{chl}), here set to a^*_{chl} = 0.014 $m^2 mg^{-1}$. The original algorithm was calibrated for ENVISAT/MERIS bands using samples from the Markermeer, IJsselmeer and the Belgian coastal zone. Some impact of the spectral differences between MERIS and MSI is expected, but was found to be small (Vanhellemont and Ruddick, 2016) using the CoastColour simulated dataset (Nechad et al., 2015).

2.6. Sensor intercomparison

No in situ data corresponding to the image dates are available, but three days with cloud-free same-day L8/OLI and S2A/MSI imagery are available: 2016-05-01, 2016-05-08, and 2016-07-20. This presents a good opportunity to perform a sensor (and atmospheric correction) intercomparison, and examine consistency of the systems. Two images were captured during early dredging operations (1st and 8th of May 2016, resp. ~20 and ~1 minutes apart), showing large dredging plumes in the direction of the main (wind driven) current. The third image was captured on the 20th of July 2016 (~20 minutes apart), after emergence of a large part of the constructed sand bars. Images were collocated on a 10 m grid, using nearest-neighbour resampling. Similar bands present on both sensors (2x blue, 1x green, 1x red, 1x NIR) were compared using density scatterplots (2D histograms), linear correlation statistics, and difference maps.

3. Results and Discussion

3.1. Temporal coverage

The combined coverage of S2A/MSI and L8/OLI was examined for the Markermeer, which is covered by two relative orbits of S2A (008 and 051) and by two paths of L8 (198 and 199). For the five month period between 2016-04-01 and 2016-09-30 this gives a theoretical total of 60 images, of which 37 from S2A and 23 from L8. Of the total possible S2A acquisitions, 4 were unavailable from the public distribution channels at the time of writing. Of the remaining 33 S2A images, 11 provided an unobscured view of the site, as did 5 of total 23 L8 images. Of these 16 total cloud-free scenes, 6 are from 3 days (2016-05-01, 2016-05-08, and 2016-07-20) where both sensors made an acquisition, and 10 are from unique days, resulting in a time-series of 13 days. The average time between cloud-free images was 33.75 days for L8, 29.5 days for S2A and 15 days for the constellation (not counting the same-day images). The

minimum time between images was 7, 3, and 2 days for L8, S2A, and the constellation respectively. The maximum time between images was reduced from 57 and 60 days from L8 and S2A to 54 days for the constellation. The effect of cloud coverage on passive optical satellite imagery is evident, and typically with a higher acquisition frequency, a higher success of a cloud-free observation can be obtained. However, as is evident from the stable maximum time between images for both satellites and the constellation, an increased revisit time will not improve coverage during cloudy or overcast periods. If a good correspondence between the data from both sensors can be established, they can be combined in monitoring of small-scale activities and phenomena.

3.2. Time series

The time-series of thirteen cloud-free scenes from both sensors is shown in Fig. 2. The first images show early dredging operations (Fig. 2a to 2c), with a small extent of the dredging plume, and a high background turbidity. During more intense dreding operations (Fig. 2d to 2f), more extensive dredging plumes were observed. In the middle of the summer the outline of the new island becomes visible (Fig. 2g to 2i). Turbidity maps derived from the NIR bands (865 nm for L8/OLI and 835 nm for S2/MSI) are shown in Fig. 3. The background turbidity in the Markermeer decreases from ~60-80 FNU in April to ~15 FNU in summer. Turbidities exceeding 120 FNU are found in the large dredging plumes observed on 2016-05-01 and 2016-05-08 (Fig. 3d and 3e). Turbidity is consistently high in the newly formed water bodies within the Marker Wadden island, but the waters change from being sediment-dominated on 2016-07-04 (Fig. 3g) to being bloom dominated later in the summer (see also section 3.3). Difficulties with haze, cloud, and cloud shadow masking are evident on 2016-05-11 (3e), 2016-07-04 (3g) and 2016-07-10 (3h), as well as problems with glint in the south-east of the scene on 2016-07-20 (3i).

3.3. High resolution chlorophyll maps

Maps of chlorophyll a concentration derived using the red and red-edge bands (Gons et al., 2005) on S2A/MSI are given in Fig. 4. An algal bloom is observed in the Markermeer (west of the Houtribdijk) in April, lasting to early May (Fig. 4a to 4d) with chlorophyll a concentrations of 50-60 $\mu g/l$. A second bloom in the Markermeer is observed in the second half of September (Fig. 4l and 4m), with lower chlorophyll a concentrations of 15-20 $\mu g/l$. In the IJsselmeer, to the east of the Houtribdijk, an intense bloom is observed in the second half of the summer (Fig. 4i to 4m) with chlorophyll a concentrations >100 $\mu g/l$. These blooms impact the NIR ρ_w and hence also the retrieved turbidity, and their effects can be seen in the turbidity time-series in Fig. 3. Note that the chlorophyll a retrieval is not impacted by the very high turbidities in the dredging plumes on 2016-05-01 (Fig. 3d and 4d) and 2016-05-08 (Fig. 3e and 4e). Values retrieved using S2A/MSI correspond well to the typical chlorophyll ranges reported by Vos et al. (2003): 10–120 $\mu g/l$ in the IJsselmeer, and an average of 64 $\mu g/l$ in the Markermeer for 2001-2002.

High chlorophyll a concentrations (>100 $\mu g/l$) are also found in the newly closed off water bodies in the artificial Marker Wadden island from 2016-07-20 to the end of summer (Fig. 4i to 4m). This can possibly be linked to a temporary reduction of turbidity in these new water bodies, probably caused by the disconnection from the wind driven currents and sediment resuspension in the Markermeer, with the increased transparency leading to an increase of phytoplankton productivity. For example, for the north-western newly formed water body, high turbidities are found on 2016-07-04 (Fig. 3g) which decrease towards 2016-07-10 (Fig. 3h). On 2016-07-20, the turbidity (i.e. NIR water reflectance) increases again (Fig. 3i) and remains relatively high during the summer. The observed chlorophyll concentration in this water body is low on 2016-07-10 (Fig. 4h) and sharply increases on 2016-07-20 (Fig. 4i) and remains high through the summer to (Fig. 4i to 4m).

3.4. Sensor intercomparison

Images from both sensors were available on 2016-05-01, 2016-05-08, and 2016-07-20, with a time difference of ~1 minute on 2016-05-08 and of ~20 minutes on the other days. The sun position, atmospheric and water conditions can hence be considered to be almost identical in both images, allowing for an intercomparison of both sensors. The sensors have near-nadir viewing conditions, except on 2016-05-08, where the region was captured near the edge of the OLI swath (and hence with a viewing zenith angle of ~8°). Scatterplots and difference maps for one of the images with the largest temporal difference (2016-05-01) are given in Fig. 5 and 6. The scatter plots show a good correspondence of ρ_w retrieved from both sensors, even with the differences in spectral response of the relatively wide bands in both sensors. Values are situated around the 1:1 line, with Reduced Major Axis (RMA) regression slopes close to 1, and small offsets.

The largest absolute differences are found for the 483:497 nm and 655:665 nm band comparisons. In

these bands, there is a large mis-match in spectral response, combined with changing spectral features typically found in turbid waters. This is for example quite clear in the different performance east (IJsselmeer) and west (Markermeer) of the Houtribdijk. In the 483:497 comparison (Fig. 5b), OLI observes significantly higher values in the (relatively clear) IJsselmeer compared to MSI, while in the 655:664 comparison (Fig. 5d) the sensors are much closer to each other. In the more turbid Markermeer, OLI observed higher reflectances than MSI in both the 483:497 and 655:664 comparisons. In the other band comparisons, the sensors observe similar reflectances both east and west of the Houtribdijk.

Some of the scatter in the intercomparison is caused by random noise in the sensor, but there is likely also a contribution of random variability in the water surface (wave facets) in the time between acquisitions. The intercomparison is affected by sensor artifacts, for example the stripe across the image starting in the North-East corner (visible in the difference plots in Fig. 6). This stripe corresponds to an edge of a detector array, and is mainly a result of the signal changes between the SWIR detectors, used in the atmospheric correction. A performance difference between the area east and west of this stripe can be observed (especially in Fig. 6e).

Another source of differences in the comparison is caused by spatial resolution, mainly near objects and land pixels. For example, the dredging ships and booms are better resolved spatially on MSI imagery, than on OLI imagery. These objects are bright across the spectrum, but don't have a strong enough SWIR signal to be removed by the cloud masking. Due to the spatial resolution of MSI, these pixels have a much larger reflectance on MSI images than on OLI images. This effect can be seen in the blue patches in the middle of the images in Fig. 6, where an halo along the dikes and islands is also present.

In general, a good agreement between the sensors was found, however it is clear that the comparison is impacted by the spectral differences between the sensor bands. Even though the temporal offset between the images is small (20 minutes), the spatial patterns of the dredging plume have sufficiently changed to impact the intercomparison.

4. Conclusions

- The ACOLITE atmospheric correction was updated to include processing of S2A/MSI imagery. S2A/MSI and L8/OLI imagery is freely available from the space agencies, which, combined with the public availability of the ACOLITE processor, allows for rapid uptake and use of the new high resolution remote sensors within the remote sensing and water quality communities.

- Using near-coincident imagery we evaluated the performance of the S2A/MSI and L8/OLI sensors and the ACOLITE atmospheric correction. Consistent water leaving reflectances were retrieved from both sensors, and good correspondence was found for the common bands. This indicates a comparable calibration of both sensors, and good atmospheric correction performance. In general, performance issues could be attributed to several effects: the different relative spectral response functions and radiometric performance of the bands, image collocation and resolution differences, presence of a low range in the signal (especially for NIR bands), variability in the sensor and sun view geometry over the scene and across the detectors on the pushbroom instruments, and even the temporal difference (20 minutes) between image acquisitions.

- The red-edge band on S2A/MSI allows for the quantification of the chlorophyll a absorption in the red band, and hence mapping of chlorophyll a concentration at unprecedented spatial and temporal scales. Thanks to this high spatial resolution (20 m), mapping of chlorophyll a concentration in highly productive near-shore coastal waters and inland waters is now a possibility, aiding EU countries in the monitoring requirements for the WFD.

Acknowledgments

This work was funded by the European Union's Seventh Framework Programme for Research (FP7/2007-2013) under grant agreement number 606797 (HIGHROC project). USGS and NASA are thanked for the Landsat 8 imagery, ESA and Copernicus are thanked for Sentinel-2A imagery. ACOLITE users are thanked for their feedback on the software.

5. References

Baeye, M., Quinn, R., Deleu, S., Fettweis, M., 2016. Detection of shipwrecks in ocean colour satellite imagery. Journal of Archaeological Science 66, 1–6.

Barnes, B. B., Hu, C., 2016. Island building in the South China Sea: detection of turbidity plumes and artificial islands using Landsat and MODIS data. Scientific Reports 6.

Barnes, B. B., Hu, C., Kovach, C., Silverstein, R. N., 2015. Sediment plumes induced by the Port of Miami dredging: Analysis and interpretation using Landsat and MODIS data. Remote Sensing of Environment 170, 328–339.

Brando, V., Braga, F., Zaggia, L., Giardino, C., Bresciani, M., Matta, E., Bellafiore, D., Ferrarin, C., Maicu, F., Benetazzo, A., et al., 2015. High-resolution satellite turbidity and sea surface temperature observations of river plume interactions during a significant flood event. Ocean Science 11 (6), 909.

Concha, J. A., Schott, J. R., 2016. Retrieval of color producing agents in Case 2 waters using Landsat 8. Remote Sensing of Environment 185, 95–107.

Eleveld, M. A., 2012. Wind-induced resuspension in a shallow lake from Medium Resolution Imaging spectrometer (MERIS) full-resolution reflectances. Water Resources Research 48 (4).

ESA/Copernicus, 2016. Sentinels Scientific Data Hub. https://scihub.copernicus.eu/, Accessed: 2016-09-22.

Franz, B. A., Bailey, S. W., Kuring, N., Werdell, P. J., 2015. Ocean color measurements with the Operational Land Imager on Landsat-8: implementation and evaluation in SeaDAS. Journal of Applied Remote Sensing 9 (1), 096070–096070.

Gons, H. J., Rijkeboer, M., Ruddick, K. G., 2005. Effect of a waveband shift on chlorophyll retrieval from MERIS imagery of inland and coastal waters. Journal of Plankton Research 27 (1), 125–127.

Kelderman, P., Ang'weya, R., De Rozari, P., Vijverberg, T., 2012. Sediment characteristics and wind-induced sediment dynamics in shallow Lake Markermeer, the Netherlands. Aquatic sciences 74 (2), 301–313.

Lammens, E., 1999. Het voedselweb van IJsselmeer en Markermeer: Veldgegevens, hypotheses, modellen en scenario's. Ministerie van Verkeer en Waterstaat, Directoraat-Generaal Rijkswaterstaat, RIZA Rijksinstituut voor Integraal Zoetwaterbeheer en Afvalwaterbehandeling.

Natuurmonumenten, 2016. Marker Wadden. https://www.natuurmonumenten.nl/marker-wadden/english/, Accessed: 2016-09-22.

Nechad, B., Ruddick, K., Neukermans, G., 2009. Calibration and validation of a generic multisensor algorithm for mapping of turbidity in coastal waters. In: SPIE Europe Remote Sensing. International Society for Optics and Photonics, p. 74730H.

Nechad, B., Ruddick, K., Schroeder, T., Oubelkheir, K., Blondeau-Patissier, D., Cherukuru, N., Brando, V., Dekker, A., Clementson, L., Banks, A. C., et al., 2015. CoastColour Round Robin data sets: a database to evaluate the performance of algorithms for the retrieval of water quality parameters in coastal waters. Earth System Science Data 7 (2), 319–348.

Noordhuis, R., 2014. Waterkwaliteit en ecologische veranderingen in het Markermeer-IJmeer. Landschap 31 (1), 13–22.

Noordhuis, R. r., 2010. Ecosysteem IJsselmeergebied: nog altijd in ontwikkeling. Rapport, RWS, Lelystad.

Ody, A., Doxaran, D., Vanhellemont, Q., Nechad, B., Novoa, S., Many, G., Bourrin, F., Verney, R., Pairaud, I., Gentili, B., 2016. Potential of High Spatial and Temporal Ocean Color Satellite Data to Study the Dynamics of Suspended Particles in a Micro-Tidal River Plume. Remote Sensing 8 (3), 245.

Pahlevan, N., Lee, Z., Wei, J., Schaaf, C. B., Schott, J. R., Berk, A., 2014. On-orbit radiometric characterization of OLI (Landsat-8) for applications in aquatic remote sensing. Remote Sensing of Environment 154, 272–284.

Toming, K., Kutser, T., Laas, A., Sepp, M., Paavel, B., Nõges, T., 2016. First Experiences in Mapping Lake Water Quality Parameters with Sentinel-2 MSI Imagery. Remote Sensing 8 (8), 640.

USGS, 2016. EarthExplorer. http://earthexplorer.usgs.gov/, Accessed: 2016-09-22.

Vanhellemont, Q., Ruddick, K., 2014. Turbid wakes associated with offshore wind turbines observed with Landsat 8. Remote Sensing of Environment 145, 105–115.

Vanhellemont, Q., Ruddick, K., 2015. Advantages of high quality SWIR bands for ocean colour processing: Examples from Landsat-8. Remote Sensing of Environment 161, 89–106.

Vanhellemont, Q., Ruddick, K., 2016. ACOLITE For Sentinel-2: Aquatic Applications of MSI imagery. In: ESA Special Publication 740. Presented at the ESA Living Planet Symposium held in Prague, Czech Republic.

Vos, R., Hakvoort, J., Jordans, R., Ibelings, B. W., 2003. Multiplatform optical monitoring of eutrophication in temporally and spatially variable lakes. Science of the Total Environment 312 (1), 221–243.

Wang, M., Shi, W., 2006. Cloud masking for ocean color data processing in the coastal regions. IEEE Transactions on Geoscience and Remote Sensing 44 (11), 3196–3105.

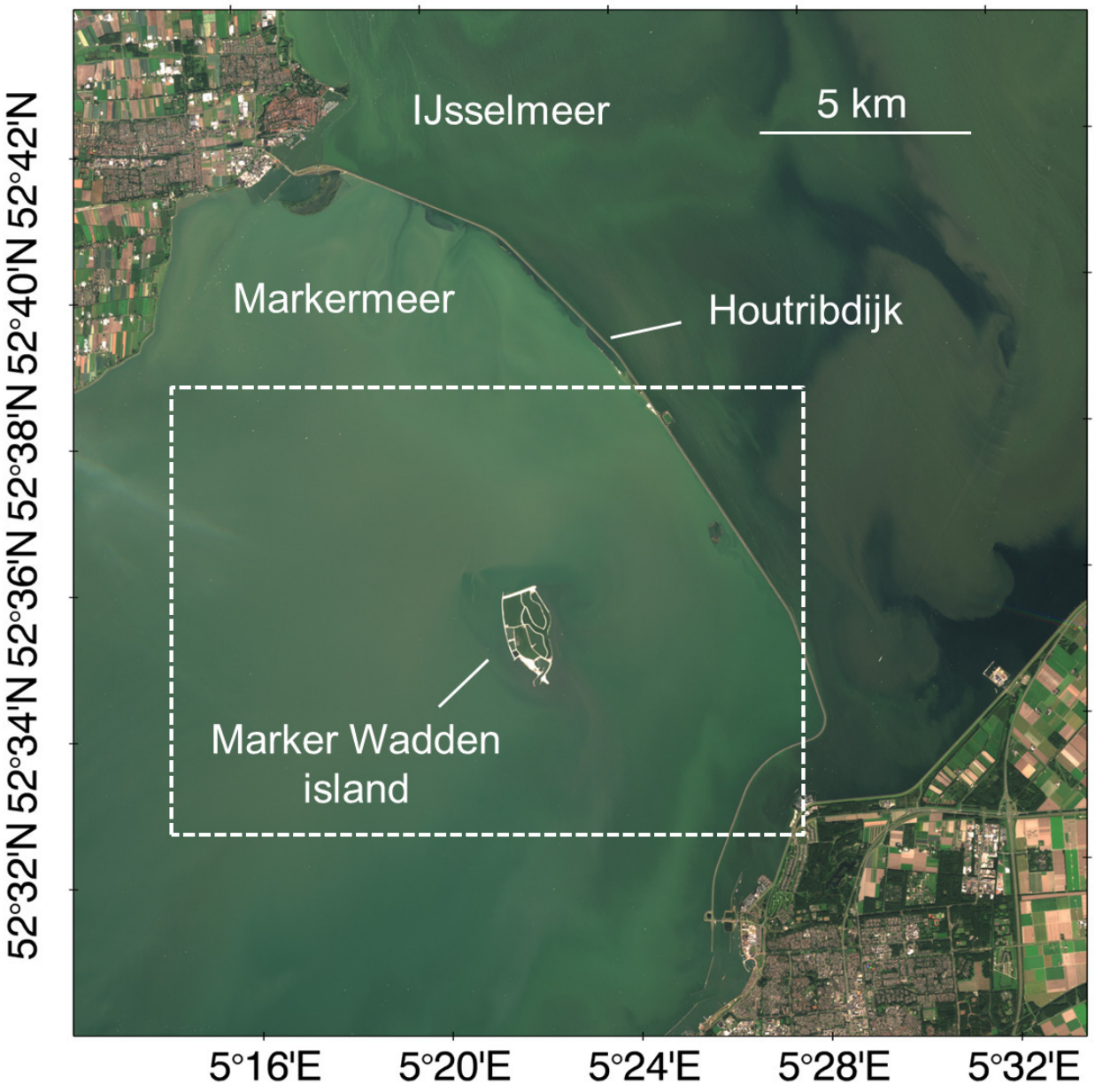

Figure 1: RGB composite showing the Markermeer and the IJsselmeer, as captured by Sentinel-2A/MSI on 2016-09-25 (10:40 UTC). The dashed rectangle shows the Marker Wadden island study area for the following figures.

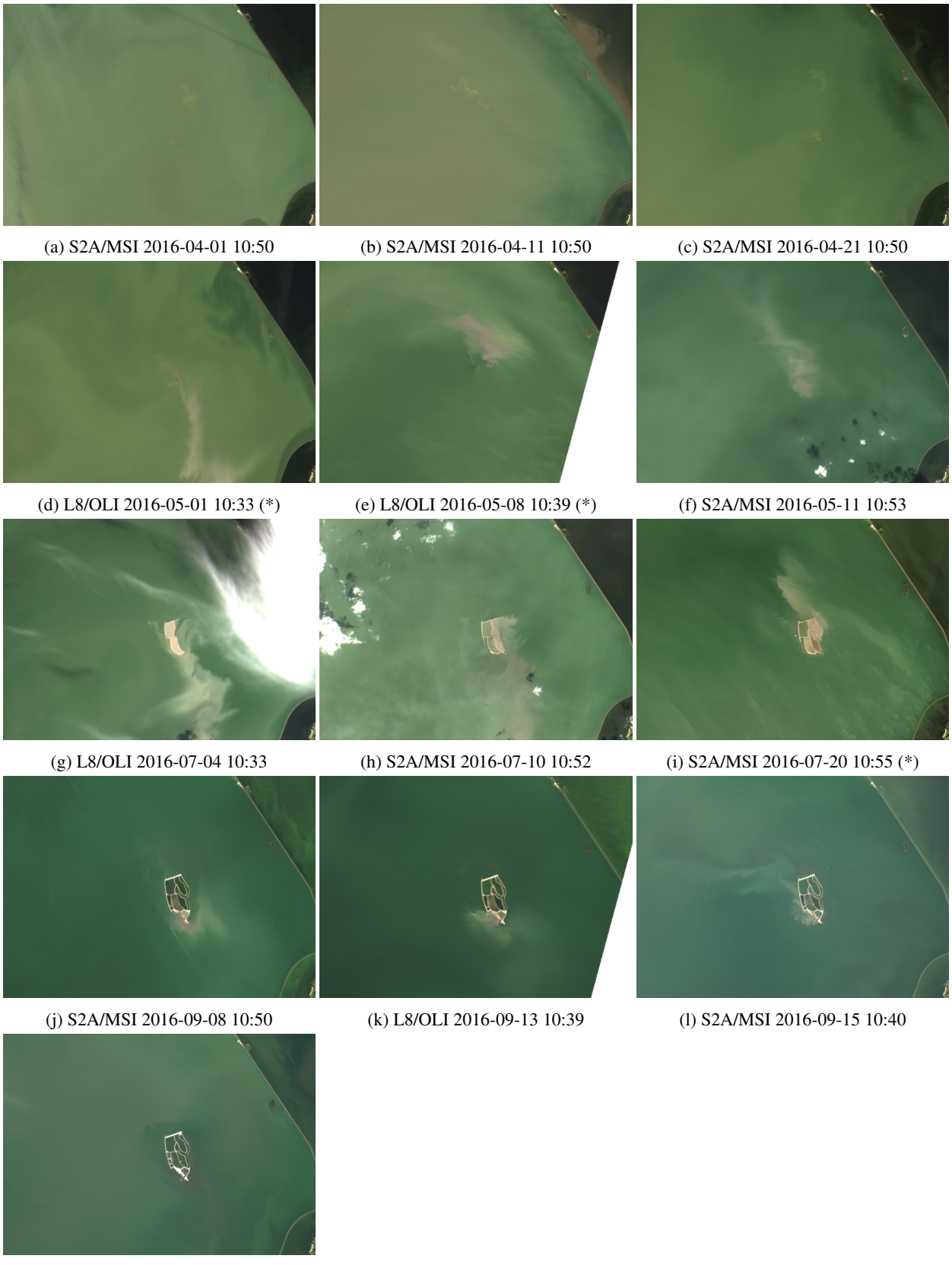

(a) S2A/MSI 2016-04-01 10:50 (b) S2A/MSI 2016-04-11 10:50 (c) S2A/MSI 2016-04-21 10:50

(d) L8/OLI 2016-05-01 10:33 (*) (e) L8/OLI 2016-05-08 10:39 (*) (f) S2A/MSI 2016-05-11 10:53

(g) L8/OLI 2016-07-04 10:33 (h) S2A/MSI 2016-07-10 10:52 (i) S2A/MSI 2016-07-20 10:55 (*)

(j) S2A/MSI 2016-09-08 10:50 (k) L8/OLI 2016-09-13 10:39 (l) S2A/MSI 2016-09-15 10:40

(m) S2A/MSI 2016-09-25 10:40

Figure 2: RGB composites for the cloud-free images acquired by S2A/MSI and L8/OLI between 2016-04-01 and 2016-09-30, showing the construction of the Marker Wadden island and associated dredging plumes. A second observation from the other sensor is available for days marked with (*). Note the cyanobacterial bloom occurring to the east of the Houtribdijk in the IJsselmeer at the end of summer (especially 2j and 2k).

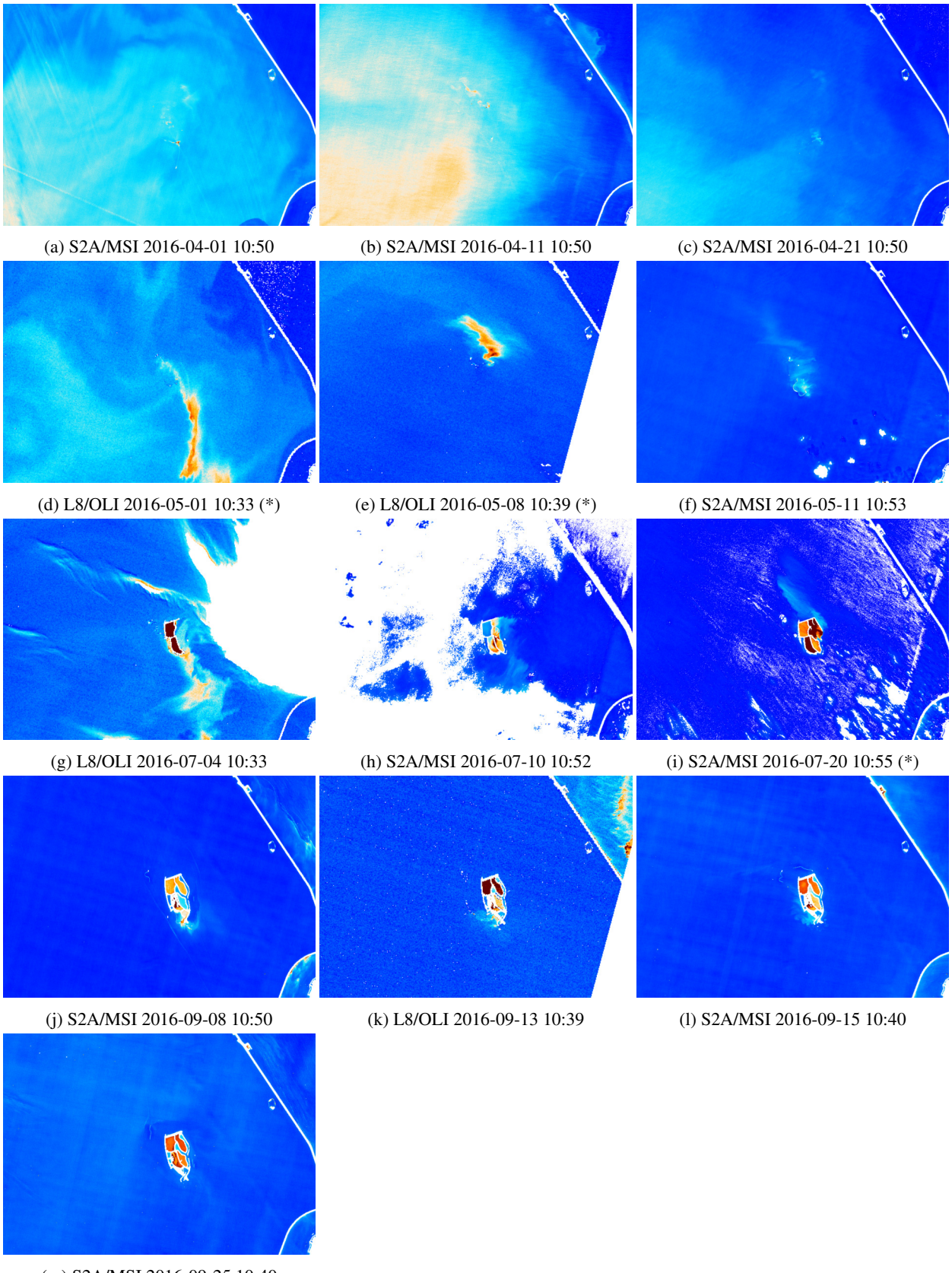

(a) S2A/MSI 2016-04-01 10:50 (b) S2A/MSI 2016-04-11 10:50 (c) S2A/MSI 2016-04-21 10:50

(d) L8/OLI 2016-05-01 10:33 (*) (e) L8/OLI 2016-05-08 10:39 (*) (f) S2A/MSI 2016-05-11 10:53

(g) L8/OLI 2016-07-04 10:33 (h) S2A/MSI 2016-07-10 10:52 (i) S2A/MSI 2016-07-20 10:55 (*)

(j) S2A/MSI 2016-09-08 10:50 (k) L8/OLI 2016-09-13 10:39 (l) S2A/MSI 2016-09-15 10:40

(m) S2A/MSI 2016-09-25 10:40

Figure 3: Turbidity derived from the NIR band for the cloud-free images acquired by S2A/MSI (835 nm) and L8/OLI (865 nm) between 2016-04-01 and 2016-09-30. The background turbidity in the Markermeer decreases towards summer. High turbidities are found in the dredging plumes. Areas masked in white are clouds, land, objects and glint. A second observation from the other sensor is available for days marked with (*).

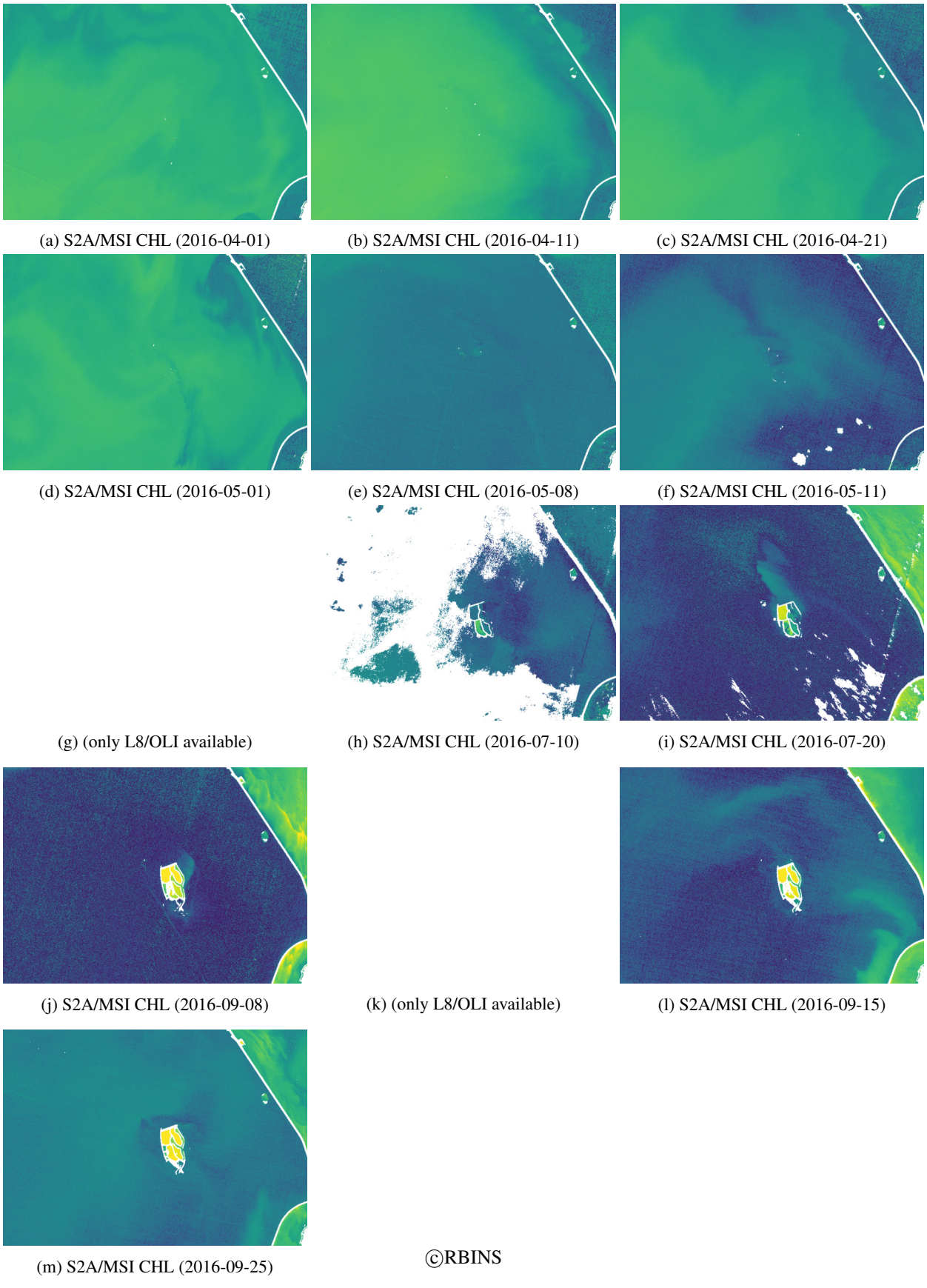

(a) S2A/MSI CHL (2016-04-01) (b) S2A/MSI CHL (2016-04-11) (c) S2A/MSI CHL (2016-04-21)

(d) S2A/MSI CHL (2016-05-01) (e) S2A/MSI CHL (2016-05-08) (f) S2A/MSI CHL (2016-05-11)

(g) (only L8/OLI available) (h) S2A/MSI CHL (2016-07-10) (i) S2A/MSI CHL (2016-07-20)

(j) S2A/MSI CHL (2016-09-08) (k) (only L8/OLI available) (l) S2A/MSI CHL (2016-09-15)

(m) S2A/MSI CHL (2016-09-25)

Figure 4: Chlorophyll a concentration derived from S2A/MSI imagery using the algorithm of Gons et al. (2005). A strong algal bloom occurs in the Markermeer in April (4a to 4d) and near the end of September (4l and 4m). A bloom is observed in the IJsselmeer at the end of the summer (4i to 4m). High chlorophyll a concentrations are found in the newly formed water bodies in the Marker Wadden island (4i to 4m).

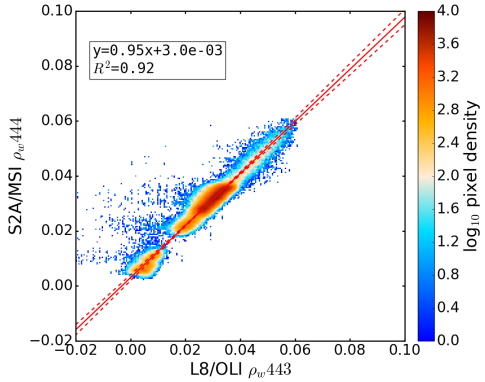

(a) L8/OLI ρ_w^{443} - S2A/MSI ρ_w^{444} (2016-05-01)

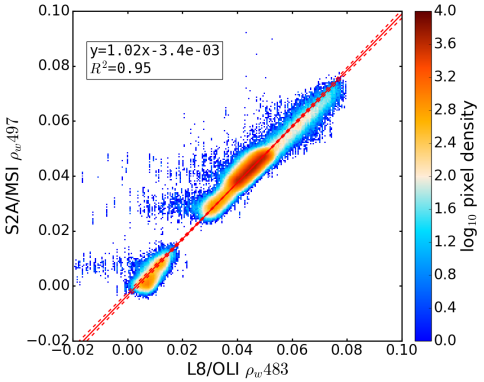

(b) L8/OLI ρ_w^{483} - S2A/MSI ρ_w^{497} (2016-05-01)

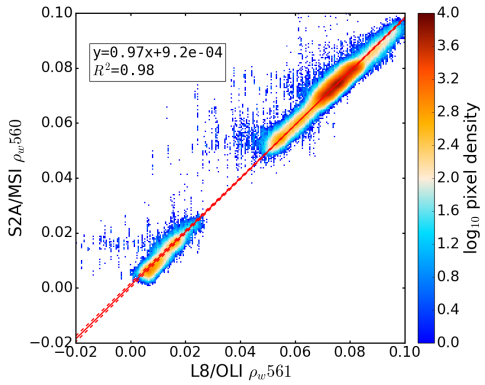

(c) L8/OLI ρ_w^{561} - S2A/MSI ρ_w^{560} (2016-05-01)

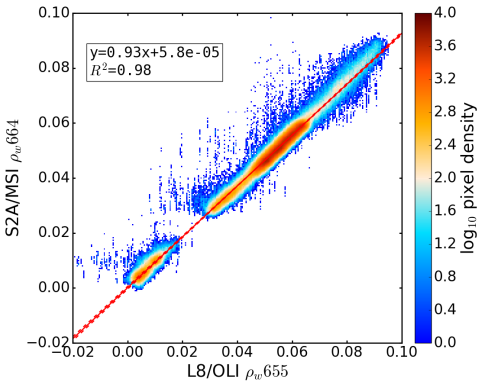

(d) L8/OLI ρ_w^{655} - S2A/MSI ρ_w^{664} (2016-05-01)

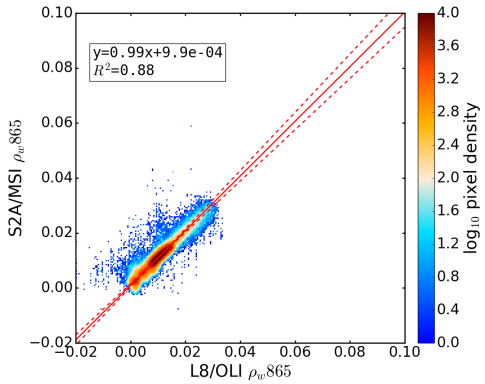

(e) L8/OLI ρ_w^{865} - S2A/MSI ρ_w^{865} (2016-05-01)

Figure 5: Comparison of ρ_w from same-day L8/OLI and S2A/MSI imagery on 2016-05-01. Colour denotes pixel density in the 2D histogram (256 horizontal and vertical bins). The solid red line is the reduced major axis regression line, i.e. the line bissecting the two ordinary least squares regression lines (dashed lines).

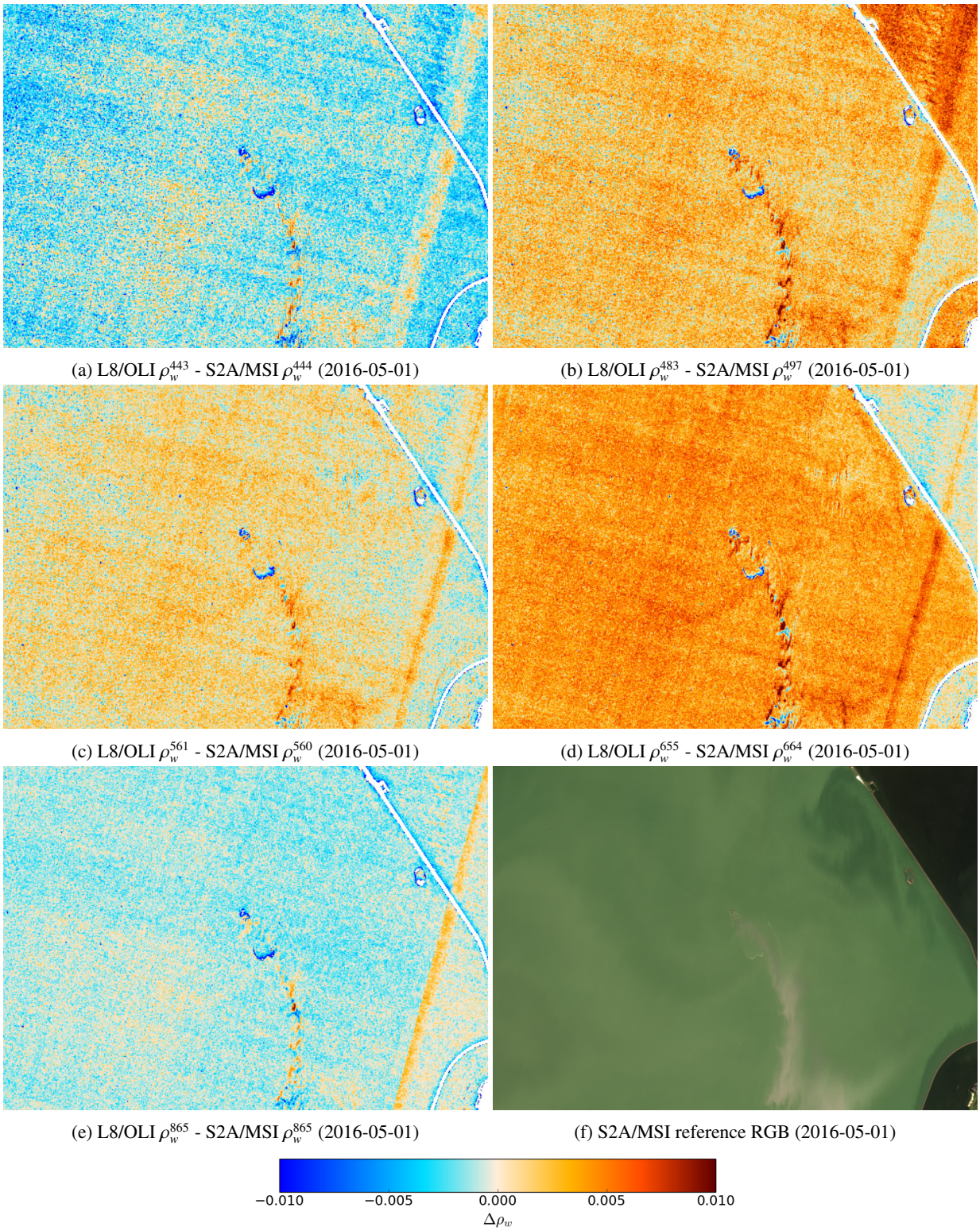

(a) L8/OLI ρ_w^{443} - S2A/MSI ρ_w^{444} (2016-05-01)

(b) L8/OLI ρ_w^{483} - S2A/MSI ρ_w^{497} (2016-05-01)

(c) L8/OLI ρ_w^{561} - S2A/MSI ρ_w^{560} (2016-05-01)

(d) L8/OLI ρ_w^{655} - S2A/MSI ρ_w^{664} (2016-05-01)

(e) L8/OLI ρ_w^{865} - S2A/MSI ρ_w^{865} (2016-05-01)

(f) S2A/MSI reference RGB (2016-05-01)

Figure 6: ρ_w difference maps from same-day L8/OLI and S2A/MSI imagery on 2016-05-01. 6f shows the S2A/MSI RGB composite. Random noise contributes to the observed differences in ρ_w, but also sensor artifacts (e.g. the stripe across the image), differences in spatial resolution (e.g. the impacts of the dredging ships and booms in the middle of the image), and differences in spectral response of the bands (e.g. difference for the Marker and IJssel lakes in 6b and 6d).